




Centrum voor Wiskunde en Informatica

View metadata, citation and similar papers at core.ac.uk

brought to you by  CORE

provided by CWI's Instituut

REPORTRAPPORT

MAS

Modelling, Analysis and Simulation



Modelling, Analysis and Simulation

Spatio-temporal patterns in a semiconductor-gas-discharge system: stability analysis and full numerical solutions

I.R. Rafatov, D.D. Šijačić, U. Ebert

REPORT MAS-E0620 AUGUST 2006

Centrum voor Wiskunde en Informatica (CWI) is the national research institute for Mathematics and Computer Science. It is sponsored by the Netherlands Organisation for Scientific Research (NWO). CWI is a founding member of ERCIM, the European Research Consortium for Informatics and Mathematics.

CWI's research has a theme-oriented structure and is grouped into four clusters. Listed below are the names of the clusters and in parentheses their acronyms.

Probability, Networks and Algorithms (PNA)

Software Engineering (SEN)

Modelling, Analysis and Simulation (MAS)

Information Systems (INS)

Copyright © 2006, Stichting Centrum voor Wiskunde en Informatica
P.O. Box 94079, 1090 GB Amsterdam (NL)
Kruislaan 413, 1098 SJ Amsterdam (NL)
Telephone +31 20 592 9333
Telefax +31 20 592 4199

ISSN 1386-3703

Spatio-temporal patterns in a semiconductor-gas-discharge system: stability analysis and full numerical solutions

ABSTRACT

A system of gas discharge and semiconductor layer forms spatial and temporal patterns spontaneously when a DC voltage is applied. The system is modeled here with a simple glow discharge model for positive ions, electrons and electric field, and the semiconductor is approximated as a linear conductor. This model in previous work has reproduced the diagram for the phase transition from homogeneous stationary to homogeneous oscillating states semi-quantitatively. In the present work, the formation of spatial patterns is investigated, both through linear stability analysis and through numerical simulations of the initial-value problem. The two methods show very good agreement. They show the onset of spatio-temporal patterns for high semiconductor resistance in agreement with experiments. The parameter dependence of temporal or spatio-temporal pattern formation is discussed in detail.

2000 Mathematics Subject Classification: 35L45

Keywords and Phrases: pattern formation, barrier discharge, stability analysis, numerical solutions

Note: This work started when both Rafatov and Sijacic were employed at CWI within theme MAS3 on an ERCIM fellowship and a PhD position by FOM. The paper was submitted to *Phys. Rev. E*.

Spatio-temporal patterns in a semiconductor-gas-discharge system: stability analysis and full numerical solutions

Ismail R. Rafatov^{1,2}, Danijela D. Šijačić^{2,3}, and Ute Ebert^{2,4*}

¹ *Dept. Physics, Middle East Technical University, TR-06531 Ankara, Turkey,*

² *CWI, P.O.Box 94079, 1090 GB Amsterdam, The Netherlands,*

³ *Dept. Applied Earth Sciences, Delft Univ. Techn., The Netherlands, and*

⁴ *Dept. Physics, Eindhoven Univ. Techn., The Netherlands.*

(Dated: August 22, 2006)

A system of gas discharge and semiconductor layer forms spatial and temporal patterns spontaneously when a DC voltage is applied. The system is modeled here with a simple glow discharge model for positive ions, electrons and electric field, and the semiconductor is approximated as a linear conductor. This model in previous work has reproduced the diagram for the phase transition from homogeneous stationary to homogeneous oscillating states semi-quantitatively. In the present work, the formation of spatial patterns is investigated, both through linear stability analysis and through numerical simulations of the initial-value problem. The two methods show very good agreement. They show the onset of spatio-temporal patterns for high semiconductor resistance in agreement with experiments. The parameter dependence of temporal or spatio-temporal pattern formation is discussed in detail.

PACS numbers: 52.80.-s, 05.45.-a, 47.54.-r, 51.50.+v

I. INTRODUCTION

Spontaneous pattern formation is a general feature in the natural and technical sciences in systems far from equilibrium [1]. The present work deals with a simple gas discharge system whose external boundary conditions allow a homogeneous stationary state, however, the system spontaneously forms spatial and temporal structures, similarly to, e.g., the classical example of Rayleigh-Bénard convection. The aim of the work is the quantitative prediction of the formed structures.

More specifically, we consider a layer of gas discharge sandwiched with a semiconductor layer between planar electrodes to which a DC voltage is applied. The system is sketched in Fig. 1; and we refer to the experiments described in [2, 3, 4, 5, 6, 7, 8, 9, 10, 11, 12, 13, 14, 15]. There the transversal extension in the x direction was so large that patterns could form spontaneously in the transversal direction without being immediately affected by the lateral boundaries. These experiments showed that the system can show a rich variety of structures: homogeneous stationary and oscillating modes, and patterns with spatial and spatio-temporal structure (stripes, spots, spirals in the plane orthogonal to the layers) [16]. For some physical mechanisms for the structures, we refer, e.g., to [17, 18].

In previous work [19, 20], we concentrated on the purely temporal oscillations that occur in a spatially homogeneous mode, therefore the analysis was restricted to the direction normal to the layers, assuming homogeneity in the transversal direction. The results presented in [19] showed that a simple two-component

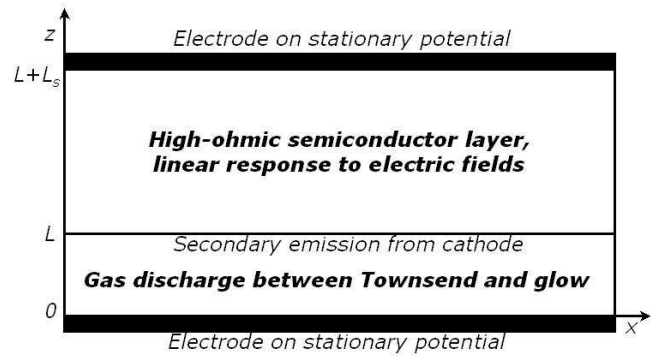


FIG. 1: Scheme of the layers of semiconductor and gas discharge sandwiched between electrodes with DC voltage.

reaction-diffusion approximation for current and voltage in the gas discharge layer can not be sufficient to describe the oscillations, though such a model is suggested through phenomenological analogies with pattern forming systems like Belousov-Zhabotinski reaction, Rayleigh-Bénard convection, patterns in bacterial colonies etc. In [20], we predicted the phase transition diagram from a homogeneous stationary to a homogeneous oscillating state. These predictions were in semi-quantitative agreement with the experiments described in [3].

While our previous work dealt with the stationary solutions [22, 23] or the dynamics in the single direc-

*Electronic address: rafatov@metu.edu.tr, ebert@cwi.nl

tion orthogonal to the layers [19, 20], we here include the transversal direction into analysis and simulations. In particular, the experimental paper [4] and thesis [6] describe that the system from [4] never forms time-independent, but spatially structured modes. Rather, starting from a homogeneous stationary state, either the homogeneous oscillating state from [20] is reached, or a spatially structured time-dependent state. Furthermore, for high semiconductor resistivity, typically a spatially structured oscillating state is reached while for low resistivity, the oscillating structures are homogeneous in the transversal direction. The resistivity could be changed by photo-illumination. Within the present paper we investigate whether we can predict this transition as well from the analysis of our simple model for gas discharge and semiconductor layer.

The paper is organized as follows. In Sec. II we introduce the model, perform dimensionless analysis, and reduce the model by adiabatic elimination of electrons. In Sec. III, the problem of linear stability analysis of the homogeneous stationary state is formulated, the equations are rewritten and numerical solution strategies are discussed. Sec. IV contains the results of the stability analysis, first the qualitative behavior of the dispersion relation as a function of the transversal wave number k , and then predictions on the parameter dependence of the dispersion relations. Sec. V presents numerical solutions of the full initial value problem and a comparison with the stability analysis results; they reveal that both methods can be trusted. Finally, Sec. VI contains discussion and conclusions. The numerical details for the full p.d.e. system are given in the appendix.

II. THE MODEL

In this section, the simplest model for the full two-dimensional glow discharge–semiconductor system is introduced. Its schematic structure is shown in Fig. 1. For the gas discharge, it contains electron and ion drift in the electric field, bulk impact ionization and secondary emission from the cathode as well as space charge effects. The semiconductor is approximated with a constant conductivity. The same physics was previously studied, e.g., in [24, 25] and in our previous papers [19, 20, 22, 23]. However, in these previous papers, any pattern formation in the transversal direction was excluded and only the single dimension orthogonal to the layers was resolved. The model then only allows for stationary solutions [22, 23] or temporal oscillations [19, 20]. We now study the onset of patterns in the direction parallel to the layers. If the layers are laterally sufficiently extended, there is rotation and translation invariance within the plane. Linear perturbations can then be decomposed into Fourier modes. These Fourier modes can be studied in a two-dimensional setting, i.e., in one direction orthogonal and one direction parallel to the layers. They are the subject of the paper.

A. Gas-discharge and semiconductor layers

The gas-discharge part of the model consists of continuity equations for two charged species, namely, electrons and positive ions with particle densities n_e and n_+ :

$$\partial_t n_e + \nabla \cdot \mathbf{\Gamma}_e = \text{source}, \quad (1)$$

$$\partial_t n_+ + \nabla \cdot \mathbf{\Gamma}_+ = \text{source}, \quad (2)$$

which are coupled to Poisson's equation for the electric field in electrostatic approximation:

$$\nabla \cdot \mathbf{E}_g = \frac{e}{\varepsilon_0} (n_+ - n_e), \quad \mathbf{E}_g = -\nabla \Phi. \quad (3)$$

Here, Φ is the electric potential, \mathbf{E}_g is the electric field in the gas discharge, e is the electron charge, and ε_0 is the dielectric constant. The vector fields $\mathbf{\Gamma}_e$ and $\mathbf{\Gamma}_+$ are the particle current densities, that in simplest approximation are described by drift only. Drift velocities are assumed to depend linearly on the local electric field with mobilities $\mu_e \gg \mu_+$:

$$\mathbf{\Gamma}_e = -\mu_e n_e \mathbf{E}_g, \quad \mathbf{\Gamma}_+ = \mu_+ n_+ \mathbf{E}_g. \quad (4)$$

Two types of ionization processes are taken into account: the α process of electron impact ionization in the bulk of the gas, and the γ process of electron emission by ion impact onto the cathode. In a local field approximation, the α process determines the source terms in the continuity equations (1) and (2):

$$\text{source} = |\mathbf{\Gamma}_e| \bar{\alpha}(|\mathbf{E}_g|), \quad \bar{\alpha}(|\mathbf{E}_g|) = \alpha_0 \alpha \left(\frac{|\mathbf{E}_g|}{E_0} \right). \quad (5)$$

We use the classical Townsend approximation

$$\alpha(|\mathbf{E}|/E_0) = \exp(-E_0/|\mathbf{E}|). \quad (6)$$

The gas discharge layer has a thickness d_g , where subscripts g or s refer to gas or semiconductor layer, respectively. The semiconductor layer of thickness d_s is assumed to have a homogeneous and field-independent conductivity $\bar{\sigma}_s$ and dielectric constant ε_s :

$$\mathbf{\Gamma}_s = \bar{\sigma}_s \mathbf{E}_s, \quad q = \varepsilon_s \varepsilon_0 \nabla \cdot \mathbf{E}_s. \quad (7)$$

B. Boundary conditions

In dimensional units, X parametrizes the direction parallel to the layers, and Z the direction orthogonal to them. The anode of the gas discharge is at $Z = 0$, the cathode end of the discharge is at $Z = d_g$, and the semiconductor extends up to $Z = d_g + d_s$. (Below, in dimensionless units, this corresponds to coordinates (x, z) and $z = 0, L, L + L_s$.)

When diffusion is neglected, the ion current and the ion density at the anode vanish. This is described by the boundary condition on the anode $Z = 0$:

$$\mathbf{\Gamma}_+(X, 0, t) = 0 \quad \Rightarrow \quad n_+(X, 0, t). \quad (8)$$

The boundary condition at the cathode, $Z = d_g$, describes the γ -process of secondary electron emission:

$$\begin{aligned} |\mathbf{\Gamma}_e(X, d_g, t)| &= \gamma |\mathbf{\Gamma}_+(X, d_g, t)| \\ \Rightarrow \mu_e n_e(X, d_g, t) &= \gamma \mu_+ n_+(X, d_g, t). \end{aligned} \quad (9)$$

Across the boundary between gas layer and semiconductor layer, the electric potential is continuous while the discontinuity of the normal electric field is determined by the surface charge

$$q_b = \left(\varepsilon_s \varepsilon_0 \mathbf{E}_s - \varepsilon_0 \mathbf{E}_g \right) \cdot \hat{\mathbf{n}}, \quad (10)$$

where $\hat{\mathbf{n}}$ is the normal vector on the boundary, directed from the gas toward the semiconductor, i.e., in the direction of growing Z . The change of surface charge in every point (X, t) of the line $Z = d_g$ is determined by the electric current densities in the adjacent gas and semiconductor layers as

$$\partial_t q_b = \left(\mathbf{\Gamma}_g - \mathbf{\Gamma}_s \right) \cdot \hat{\mathbf{n}}, \quad (11)$$

where $\mathbf{\Gamma}_g$ and $\mathbf{\Gamma}_s$ are the current densities at $Z = d_g \pm 0$ in gas and semiconductor. $\mathbf{\Gamma}_s$ is given in Eq. (7), $\mathbf{\Gamma}_g$ on the boundary due to condition (9) is

$$\mathbf{\Gamma}_g = e \mathbf{\Gamma}_+ - e \mathbf{\Gamma}_e \stackrel{Z=d_g}{=} (1 + \gamma) e \mu_+ n_+ \mathbf{E}_g. \quad (12)$$

Equations (10)–(12) are summarized as

$$\begin{aligned} q_b &= \left(\varepsilon_s \varepsilon_0 \mathbf{E}_s - \varepsilon_0 \mathbf{E}_g \right) \cdot \hat{\mathbf{n}} \\ &= q_b|_{t=0} + \int_0^t dt \left((1 + \gamma) e n_+ \mu_+ \mathbf{E}_g - \bar{\sigma}_s \mathbf{E}_s \right) \cdot \hat{\mathbf{n}}. \end{aligned} \quad (13)$$

This boundary condition is valid in any point (X, t) of the gas-semiconductor boundary $Z = d_g$.

Finally, a DC voltage U_t is applied to the gas-semiconductor system determining the electric potential on the outer boundaries

$$\Phi(X, 0, t) = 0, \quad \Phi(X, d_g + d_s, t) = -U_t. \quad (14)$$

Here the first potential vanishes due to gauge freedom.

C. Dimensional analysis

The dimensional analysis is performed essentially as in [19, 20, 21, 22, 23]. However, as it is useful to measure the time in terms of the ion mobility rather than the electron mobility, we introduce the intrinsic parameters of the system as

$$t_0^{(\mu)} = \frac{1}{\alpha_0 \mu_+ E_0} = \frac{t_0}{\mu}, \quad r_0 = \frac{1}{\alpha_0}, \quad q_0 = \varepsilon_0 \alpha_0 E_0. \quad (15)$$

Here time immediately is measured in units of $t_0^{(\mu)}$, while in [20], first the time scale t_0 was used. The intrinsic

dimensionless parameters of the gas discharge are the mobility ratio μ of electrons and ions and the length ratio L of discharge gap width and impact ionization length:

$$\mu = \frac{\mu_+}{\mu_e}, \quad L = \frac{d_g}{r_0}. \quad (16)$$

The dimensionless time, coordinates and fields are

$$\begin{aligned} \mathbf{r} &= \frac{\mathbf{R}}{r_0}, \quad \tau = \frac{t}{t_0^{(\mu)}}, \quad \sigma(\mathbf{r}, \tau) = \frac{e n_e(\mathbf{R}, t)}{q_0}, \\ \rho(\mathbf{r}, t) &= \frac{e n_+(\mathbf{R}, t)}{q_0}, \quad \mathcal{E}(\mathbf{r}, t) = \frac{\mathbf{E}(\mathbf{R}, t)}{E_0}. \end{aligned} \quad (17)$$

Here the dimensional \mathbf{R} is expressed by coordinates (X, Z) and the dimensionless \mathbf{r} by (x, z) .

The total applied voltage is rescaled as

$$\mathcal{U}_t = \frac{U_t}{E_0 r_0}. \quad (18)$$

The dimensionless parameters of the semiconductor are conductivity σ_s and width L_s :

$$\sigma_s = \frac{\bar{\sigma}_s}{\mu_+ q_0}, \quad L_s = \frac{d_s}{r_0}. \quad (19)$$

Note that the dimensionless conductivity is now also measured on the scale of ion mobility. Dimensionless capacitance and resistance of the semiconductor and its characteristic relaxation time are expressed in terms of these quantities as

$$\mathcal{R}_s = \frac{L_s}{\sigma_s}, \quad C_s = \frac{\varepsilon_s}{L_s}, \quad \tau_s = C_s \mathcal{R}_s = \frac{\varepsilon_s}{\sigma_s}. \quad (20)$$

D. Adiabatic elimination of electrons and final formulation of the problem

The dynamics of a glow discharge takes place through ion motion where the ions are much slower than the electrons. As in [20], the electrons therefore equilibrate on the time scale of ion motion and can hence be adiabatically eliminated: After substituting $s = \sigma/\mu$, the gas discharge part of the system has the form

$$\mu \partial_\tau s - \nabla \cdot (\mathcal{E} s) = s |\mathcal{E}| \alpha(|\mathcal{E}|), \quad (21)$$

$$\partial_\tau \rho + \nabla \cdot (\mathcal{E} \rho) = s |\mathcal{E}| \alpha(|\mathcal{E}|), \quad (22)$$

$$\nabla \cdot \mathcal{E} = \rho - \mu s, \quad \mathcal{E} = -\nabla \phi, \quad (23)$$

and in the limit of $\mu \rightarrow 0$, it becomes

$$-\nabla \cdot (\mathcal{E} s) = s |\mathcal{E}| \alpha(|\mathcal{E}|), \quad (24)$$

$$\partial_\tau \rho + \nabla \cdot (\mathcal{E} \rho) = s |\mathcal{E}| \alpha(|\mathcal{E}|), \quad (25)$$

$$\nabla \cdot \mathcal{E} = \rho, \quad \mathcal{E} = -\nabla \phi. \quad (26)$$

As in [20], the electric field \mathcal{E} is now only influenced by the ion density ρ , and not by the much smaller density of

fast electrons (since the electrons are generated in equal numbers, but leave the system much more rapidly), and the electrons s follow the ion motion instantaneously: given the electron density on the cathode $s(x, L, \tau)$ and the field distribution \mathcal{E} in the gas gap, the electron density is determined everywhere through (24). The boundary conditions (8) and (9) for electrons and ions are

$$\rho(x, 0, \tau) = 0, \quad s(x, L, \tau) = \gamma \rho(x, L, \tau). \quad (27)$$

After rescaling, the semiconductor is written as

$$\nabla \cdot \mathcal{E} = 0, \quad \mathcal{E} = -\nabla \phi, \quad \mathbf{j}_s = \sigma_s \mathcal{E}, \quad (28)$$

and the condition (13) for the charge on the semiconductor-gas boundary becomes

$$\begin{aligned} \frac{q_b}{q_0} &= \left(\varepsilon_s \mathcal{E}|_{z=L^+} - \mathcal{E}|_{z=L^-} \right) \cdot \hat{\mathbf{n}} \\ &= \frac{q_b}{q_0} \Big|_{\tau=0} + \int_0^\tau d\tau \left((1 + \gamma) \rho \mathcal{E}|_{L^-} - \sigma_s \mathcal{E}|_{L^+} \right) \cdot \hat{\mathbf{n}}. \end{aligned} \quad (29)$$

In the perturbation analysis, the differential form of charge conservation on the boundary is used

$$\partial_\tau \frac{q_b}{q_0} = \left((1 + \gamma) \rho \mathcal{E}|_{L^-} - \sigma_s \mathcal{E}|_{L^+} \right) \cdot \hat{\mathbf{n}}. \quad (30)$$

The total width of the layered structure is $L_z = L + L_s$. At its outer boundaries $z = 0$ and $z = L_z$, the electrodes are on the electric potential $\phi(x, 0, \tau) = 0$ and $\phi(x, L_z, \tau) = -\mathcal{U}_t$, respectively. Finally, in the numerical solutions of the PDEs, lateral boundaries at $x = 0$ and $x = L_x$ with periodic boundary conditions for ϕ , ρ , and s are introduced.

E. Dimensional and non-dimensional parameters

Our choice of parameters was guided by the experiments in Ref. [3, 4] and taken as previously in [20]. The experiments are performed on a discharge in nitrogen at 40 mbar in a gap of 1 mm. The semiconductor layer consists of 1.5 mm of GaAs with dielectric constant $\varepsilon_s = 13.1$. The applied voltages were in the range of 580–740 V. Through photosensitive doping, the conductivity of the semiconductor layer could be increased by an order of magnitude; the dark conductivity was $\bar{\sigma}_s = 3.2 \times 10^{-8}/(\Omega \text{ cm})$.

For the gas discharge, we used the ion mobility $\mu_+ = 23.33 \text{ cm}^2/(\text{V s})$ and electron mobility $\mu_e = 6666.6 \text{ cm}^2/(\text{V s})$, therefore the mobility ratio is $\mu = \mu_+/\mu_e = 0.0035$. For $\alpha_0 = Ap = [27.8 \mu\text{m}]^{-1}$ and for $E_0 = Bp = 10.3 \text{ kV/cm}$, we used values from [25]. The secondary emission coefficient was taken as $\gamma = 0.08$.

Therefore the intrinsic scales from (15) are

$$\begin{aligned} r_0 &= 27.8 \mu\text{m}, & t_0^{(\mu)} &= 11.6 \text{ ns}, \\ q_0 &= 2.04 \cdot 10^{12} e/\text{cm}^3, & E_0 &= 10.3 \text{ kV/cm}, \end{aligned} \quad (31)$$

the gas gap width of $d = 1 \text{ mm}$ corresponds to $L = 36$ in dimensionless units, and the semiconductor width of $d_s = 1.5 \text{ mm}$ to a dimensionless value of $L_s = 54$. The dimensionless applied voltages are in the range of $17.5 \leq \mathcal{U}_t \leq 50$, which correspond to the dimensional range of $500 \text{ V} \leq U_t \leq 1425 \text{ V}$. The dimensionless capacitance of the semiconductor is $C_s = 0.243$. We investigate the conductivity range of $6 \cdot 10^{-8}/(\Omega \text{ cm}) \leq \bar{\sigma}_s \leq 6 \cdot 10^{-7}/(\Omega \text{ cm})$ which corresponds to a semiconductor resistance \mathcal{R}_s of 700 to 7000 in the new dimensionless units (or to $2 \cdot 10^5$ to $2 \cdot 10^6$ in the units of our previous papers [19, 20]). For the lowest conductivity of $\bar{\sigma}_s = 3.2 \times 10^{-8}/(\Omega \text{ cm})$, pattern formation consistently occurs neither in our analysis nor in the experiment.

III. STABILITY ANALYSIS: METHOD

In this section, the stability analysis of the homogeneous stationary state is set up. While in earlier work [20], only temporal oscillations were admitted, here the stability with respect to temporal and spatial perturbations is analyzed. In particular, linearized equations are derived that define an eigenvalue problem, and the numerical solution strategy is discussed. It becomes particularly demanding for large wave numbers k . This forms the basis for the derivation of dispersion relations in Chapter IV.

A. Linear perturbation analysis for transversal Fourier modes: problem definition

Here the equations are derived that describe linear perturbations of the stationary state that is furthermore homogeneous in the transversal direction, in agreement with the external boundary conditions. The analysis is set up as in [20], but now also transversal perturbations are admitted. The unperturbed equations are denoted by a subscript 0, they are for $\mu \rightarrow 0$

$$\partial_z j_0 = -j_0 \alpha(\mathcal{E}_0), \quad \text{where } j_0 = s_0 \mathcal{E}_0, \quad (32)$$

$$\mathcal{E}_0 \rho_0 + j_0 = J_0, \quad \partial_z J_0 = 0, \quad (33)$$

$$\partial_z \mathcal{E}_0 = \rho_0, \quad \partial_z \phi_0 = -\mathcal{E}_0, \quad (34)$$

with boundary conditions

$$\begin{aligned} j_0(0) &= J_0, & \phi_0(0) &= 0, \\ j_0(L) &= \frac{1+\gamma}{\gamma} J_0, & \phi_0(L) &= -\mathcal{U}_0, \quad \mathcal{U}_t = \mathcal{U}_0 + \mathcal{R}_s J_0. \end{aligned} \quad (35)$$

Here J_0 is the total current and \mathcal{U}_t is the applied voltage. For a further discussion, see [20, 22, 23].

The first order perturbation theory is denoted by a subscript 1. As the transversal modes can be decomposed into Fourier modes with wavenumber k within linear per-

turbation theory, the ansatz

$$s(x, z, \tau) = s_0(z) + s_1(z) e^{ikx + \lambda\tau}, \quad (36)$$

$$\rho(x, z, \tau) = \rho_0(z) + \rho_1(z) e^{ikx + \lambda\tau}, \quad (37)$$

$$\phi(x, z, \tau) = \phi_0(z) + \phi_1(z) e^{ikx + \lambda\tau}. \quad (38)$$

is used where the perturbation is supposed to be small. Insertion of this ansatz into the equations for the gas discharge (24)–(26) yields

$$\partial_z s_1 = - \left(\alpha(\mathcal{E}_0) + \frac{\partial_z \mathcal{E}_0}{\mathcal{E}_0} \right) s_1 - \frac{s_0}{\mathcal{E}_0} \rho_1 \quad (39)$$

$$- \left(\frac{s_0}{\mathcal{E}_0} \alpha(\mathcal{E}_0) + \frac{\partial_z s_0}{\mathcal{E}_0} + s_0 \alpha'(\mathcal{E}_0) \right) \mathcal{E}_1,$$

$$\partial_z \rho_1 = \alpha(\mathcal{E}_0) s_1 - \left(\frac{\lambda + \rho_0 + \partial_z \mathcal{E}_0}{\mathcal{E}_0} \right) \rho_1 \quad (40)$$

$$+ \left(\frac{s_0}{\mathcal{E}_0} \alpha(\mathcal{E}_0) - \frac{\partial_z \rho_0}{\mathcal{E}_0} + s_0 \alpha'(\mathcal{E}_0) \right) \mathcal{E}_1,$$

$$\partial_z \mathcal{E}_1 = \rho_1 - k^2 \phi_1, \quad (41)$$

$$\partial_z \phi_1 = -\mathcal{E}_1. \quad (42)$$

Here \mathcal{E}_1 is the field perturbation in the z direction. The boundary conditions are:

$$\rho_1(0) = 0, \quad \phi_1(0) = 0, \quad s_1(L) = \gamma \rho_1(L), \quad (43)$$

where $z = L$ is the boundary between gas discharge and semiconductor layer.

In the semiconductor layer, the equation $\Delta\phi = 0$ with the boundary condition $\phi(L_z) = -\mathcal{U}_t$ at the position of the cathode $L_z = L + L_s$ has to be solved. For ϕ_1 , this means that we have to solve $\Delta\phi_1 = 0$ with $\phi_1(L_z) = 0$. This problem is solved explicitly for $L \leq z \leq L_z$ by

$$\phi_1(z) = C_1 \sinh(k(z - L_z)), \quad (44)$$

with the arbitrary coefficient C_1 . The 'jump' condition (29), (30) for the electric field on the semiconductor gas discharge boundary is expressed as

$$\begin{aligned} & -C_1 k \cosh(kL_s) [\lambda \varepsilon_s + \sigma_s] \\ & = \left[(1 + \gamma)(\rho_0 \mathcal{E}_1 + \mathcal{E}_0 \rho_1) + \lambda \mathcal{E}_1 \right]_L, \end{aligned} \quad (45)$$

after q_b is eliminated. As the potential (44) is continuous we get on the boundary $z = L^-$ of the gas discharge region

$$\phi_1(L^+) = \phi_1(L^-) = -C_1 \sinh(kL_s). \quad (46)$$

Now C_1 in (45) can be substituted by $\phi_1(L)$ through (46). The result is the second boundary condition at $z = L$

$$\phi_1(L) = \frac{(1 + \gamma)(\rho_0 \mathcal{E}_1 + \mathcal{E}_0 \rho_1) + \lambda \mathcal{E}_1}{\lambda \varepsilon_s + \sigma_s} \Big|_L \frac{\tanh(kL_s)}{k}. \quad (47)$$

Now the semiconductor is integrated out, and we are left with four first order ordinary differential equations (39)–(42) and four boundary conditions (43), (47) that together determine an eigenvalue problem for $\lambda = \lambda(k)$.

B. New fields lead to compacter equations

It is convenient to write the equations (39) in terms of the fields h and g

$$h = \frac{s_1}{s_0} + \frac{\mathcal{E}_1}{\mathcal{E}_0} \quad \text{and} \quad g = \mathcal{E}_0 \mathcal{E}_1 \quad (48)$$

as in [20]. Furthermore, for non-vanishing wave-numbers k , it is convenient to use charge conservation

$$0 = \partial_\tau \rho + \nabla \cdot (s\mathcal{E} + \rho\mathcal{E}) = \nabla \cdot (\partial_\tau \mathcal{E} + (s + \rho)\mathcal{E}) \quad (49)$$

to eliminate particle densities completely in favor of the z component of the total charge

$$j_1 = \lambda \mathcal{E}_1 + (s_1 + \rho_1)\mathcal{E}_0 + (s_0 + \rho_0)\mathcal{E}_1. \quad (50)$$

This leads to a compacter form of the system (39)–(42):

$$\partial_z h = -\frac{\alpha'}{\mathcal{E}_0} g - \frac{k^2}{\mathcal{E}_0} \phi_1, \quad (51)$$

$$\partial_z g = -j_0 h - \frac{\lambda}{\mathcal{E}_0} g + j_1 - k^2 \mathcal{E}_0 \phi_1, \quad (52)$$

$$\partial_z j_1 = -k^2 \left(\lambda + \frac{J_0}{\mathcal{E}_0} \right) \phi_1, \quad (53)$$

$$\partial_z \phi_1 = -\frac{1}{\mathcal{E}_0} g. \quad (54)$$

The boundary conditions (43) and (47) are rewritten as:

$$j_1(0) = \frac{\lambda}{\mathcal{E}_0(0)} g(0) + J_0 h(0), \quad (55)$$

$$\phi_1(0) = 0, \quad (56)$$

$$j_1(L) = \frac{\lambda}{\mathcal{E}_0(L)} g(L) + J_0 h(L), \quad (57)$$

$$\phi_1(L) = \frac{\mathcal{R}_s j_1(L) \tanh(kL_s)}{1 + \lambda \tau_s k L_s}. \quad (58)$$

Note that in the last equation, the identity $(\lambda \varepsilon_s + \sigma_s) = (1 + \lambda \tau_s) L_s / \mathcal{R}_s$ was used. Note further that the limit of $k \rightarrow 0$ of these equations reproduces the limit of $\mu \rightarrow 0$ of the analogous 1D equations in [20].

C. Formal solution and numerical implementation

In matrix form, the linearized equations (51)–(54) are

$$\partial_z \mathbf{v} = \mathbf{M}_\lambda \cdot \mathbf{v}, \quad \text{where } \mathbf{v}(z) = \begin{pmatrix} h \\ g \\ j_1 \\ \phi_1 \end{pmatrix} \quad (59)$$

$$\text{and } \mathbf{M}_\lambda(z) = \begin{pmatrix} 0 & -\alpha'/\mathcal{E}_0 & 0 & -k^2/\mathcal{E}_0 \\ -j_0 & -\lambda/\mathcal{E}_0 & 1 & -k^2 \mathcal{E}_0 \\ 0 & 0 & 0 & -k^2 (\lambda + J_0/\mathcal{E}_0) \\ 0 & -1/\mathcal{E}_0 & 0 & 0 \end{pmatrix}.$$

The matrix $\mathbf{M}_\lambda(z)$ depends on wavenumber k and eigenvalue λ . It depends on z through the functions $\mathcal{E}_0(z)$, $\alpha(\mathcal{E}_0(z))$, and $j_0(z)$.

The boundary conditions (55), (56) at $z = 0$ mean that the general solution of the linear equation can be written as a superposition of two independent solutions of (59)

$$\mathbf{v}(z) = c_1 \mathbf{v}^{(1)}(z) + c_2 \mathbf{v}^{(2)}(z), \quad \partial_z \mathbf{v}^{(i)} = \mathbf{M}_\lambda \cdot \mathbf{v}^{(i)},$$

$$\mathbf{v}^{(1)}(0) = \begin{pmatrix} 1/J_0 \\ 0 \\ 1 \\ 0 \end{pmatrix}, \quad \mathbf{v}^{(2)}(0) = \begin{pmatrix} 0 \\ \mathcal{E}_0(0)/\lambda \\ 1 \\ 0 \end{pmatrix}. \quad (60)$$

The solution (60) has to obey the boundary conditions (57) and (58) at $z = L$ as well. Denoting the components of the solutions as $\mathbf{v}^{(i)} = (h^{(i)}, g^{(i)}, j_1^{(i)}, \phi_1^{(i)})$ for $i = 1, 2$, we get

$$c_1 \left[j_1^{(1)} - \frac{\lambda}{\mathcal{E}_0} g^{(1)} - J_0 h^{(1)} \right]_{z=L} + c_2 \left[j_1^{(2)} - \frac{\lambda}{\mathcal{E}_0} g^{(2)} - J_0 h^{(2)} \right]_{z=L} = 0, \quad (61)$$

$$c_1 \left[\mathcal{R}_s j_1^{(1)} - \frac{(1 + \lambda \tau_s) k L_s}{\tanh(k L_s)} \phi_1^{(1)} \right]_{z=L} + c_2 \left[\mathcal{R}_s j_1^{(2)} - \frac{(1 + \lambda \tau_s) k L_s}{\tanh(k L_s)} \phi_1^{(2)} \right]_{z=L} = 0. \quad (62)$$

These equations have nontrivial solutions, if the determinant

$$\Delta(z) = \begin{vmatrix} j_1^{(1)} - \frac{\lambda}{\mathcal{E}_0} g^{(1)} - J_0 h^{(1)} & j_1^{(2)} - \frac{\lambda}{\mathcal{E}_0} g^{(2)} - J_0 h^{(2)} \\ \mathcal{R}_s j_1^{(1)} - \frac{(1 + \lambda \tau_s) k L_s}{\tanh(k L_s)} \phi_1^{(1)} & \mathcal{R}_s j_1^{(2)} - \frac{(1 + \lambda \tau_s) k L_s}{\tanh(k L_s)} \phi_1^{(2)} \end{vmatrix} \quad (63)$$

vanishes at $z = L$

$$\Delta(z = L) = 0. \quad (64)$$

Now for a fixed k , we start with some initial estimate for the eigenvalue $\lambda(k)$ and solve equation (60) numerically for both initial values. The next estimate for λ can be found from condition (64) since it is quadratic in λ . This process is iterated until the accuracy is sufficient. We used the condition $|\lambda^{(n+1)} - \lambda^{(n)}| / |\lambda^{(n+1)}| < 10^{-8}$ for the n 'th iteration step to finish iterations. For the stability of the iteration process under-relaxation was used. For the integration of the equations (59), we used the classic fourth-order Runge-Kutta method on a grid with 500 nodes. The majority of investigated solutions of the present problem are oscillating, therefore the eigenvalues λ are complex, and the eigenfunctions $\mathbf{v}(z)$ are complex as well. We have taken this into account by working with complex fields.

After the eigenvalue $\lambda(k)$ is found, the eigenfunction is determined by inserting the ratio

$$\frac{c_2}{c_1} = - \frac{\tanh(k L_s) \mathcal{R}_s j_1^{(1)}(L) - k L_s (1 + \lambda \tau_s) \phi_1^{(1)}(L)}{\tanh(k L_s) \mathcal{R}_s j_1^{(2)}(L) - k L_s (1 + \lambda \tau_s) \phi_1^{(2)}(L)} \quad (65)$$

into Eq. (60).

D. The numerical strategy for large k

The above method gives reliable results for small values of k and has been used to derive the results presented in Sect. IV B. However, for investigating possible instabilities for large wave number k as in Sect. IV A, e.g., for finding both solution branches for $k > \mathcal{O}(10^0)$ in Fig. 3, a better strategy is needed.

There are two points where the integration routine has to be improved for large k . There is first the fact that the matrix of coefficients is poorly conditioned. This can be seen by noting that one column is much bigger than another one. A more precise measure of numerical ill-conditioning of a matrix is provided by computing the normalized determinant of the matrix. When the normalized determinant is much smaller than unity, the matrix is ill-conditioned. The normalized determinant is obtained by dividing the value of the determinant of the matrix by the product of the absolute values of the vectors forming the rows of the matrix.

The second point is the so-called 'build-up' error. The difficulty arises because the solution (60) requires combining numbers which are large compared to the desired solution; that is $\mathbf{v}^{(1)}(z)$ and $\mathbf{v}^{(2)}(z)$ can be up to 3 orders of magnitude larger than their linear combination, which is the actual solution. Hence significant digits are lost through subtraction. This error cannot be avoided by a more accurate integration unless all computations are carried out with higher precision. Godunov [26] proposed a method for avoiding the loss of significance which does not require multi-precision arithmetics and which is based on keeping the matrix of base solutions orthogonal at each step of the integration.

A modification of Godunov's method [27], which is computationally more efficient and which yields better accuracy, is implemented in the algorithm used for large k . The main difference to the algorithm described in Section III C is that here we examine the base solutions (obtained by any standard integration method) at each mesh point and when they exceed certain nonorthogonality criteria we orthonormalize the base solution. We have to start with initial conditions that are orthogonal

to each other and not only to the boundary conditions:

$$\mathbf{v}^{(1)}(0) = \begin{pmatrix} -1 \\ -1 \\ -\frac{\lambda}{\varepsilon_0(0)} - J_0 \\ 0 \end{pmatrix},$$

$$\mathbf{v}^{(2)}(0) = \begin{pmatrix} H_0 \\ 1 \\ \frac{\lambda}{\varepsilon_0(0)} + J_0 H_0 \\ 0 \end{pmatrix},$$

where
$$H_0 = -\frac{1 + \frac{\lambda}{\varepsilon_0(0)} \left(J_0 + \frac{\lambda}{\varepsilon_0(0)} \right)}{1 + J_0 \left(\frac{\lambda}{\varepsilon_0(0)} + J_0 \right)}. \quad (66)$$

Based on the orthogonalization developed in [27], the differential equation (59) can be solved very accurately even for large k , which allows us to find the eigenvalues according to the criteria described in the previous section.

Since we must solve the matrix equation (59) several times for different values of λ , we must insist that the orthonormalization is the same for all these solutions. In essence we must insist that the determinant is uniformly scaled in order for the successive approximations for λ to be consistent. Numerically this can be accomplished by determining the set of orthonormalization points and matrices for the solution corresponding to the first initial guess for λ and thereafter applying the same matrices at the corresponding points for all successive solutions.

The program is written in C, and the integration method is one-step simple Runge-Kutta and on the domain $L=36$ the number of grid points is varied from $n=500$ to $n=18000$ depending on the range of k .

IV. STABILITY ANALYSIS: DISPERSION RELATIONS

In previous work [20], we have derived bifurcation diagrams like the one shown in Fig. 2 indicating where the homogeneous stationary state becomes unstable to homogeneous oscillations. Any lateral inhomogeneities were excluded in this earlier work. We now take this diagram as a basis and investigate which additional spatial or spatio-temporal instabilities can occur.

A. Qualitative behavior: most unstable modes with $k = 0$ or $k \neq 0$

If patterns form spontaneously in the system due to a linear instability, i.e., in a supercritical bifurcation, its signature will be found in the dispersion relation $\lambda = \lambda(k)$. More precisely, there will be a band of Fourier modes with positive growth rate $\text{Re} \lambda(k) > 0$. If the instability is purely growing without oscillations, then $\text{Im} \lambda(k) = 0$. On the other hand, oscillations cause the imaginary part of the dispersion relation to be non-vanishing: $\text{Im} \lambda(k) \neq 0$.

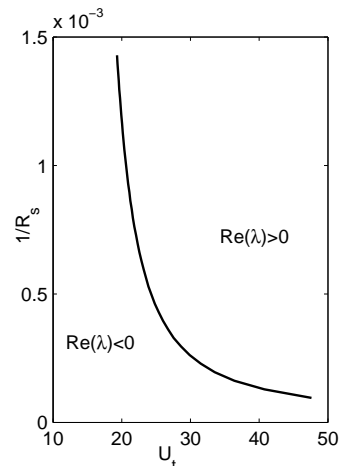


FIG. 2: The bifurcation line where the homogeneous stationary state becomes unstable to homogeneous temporal oscillations; hence structure formation in the transversal direction is here excluded. The bifurcation is drawn as a function of \mathcal{U}_t and $1/\mathcal{R}_s$ while all other parameters keep the constant values described in Sect. II E. We recall that \mathcal{R}_s can be varied by a factor of 10 by photo-illumination. The maximal value $1/\mathcal{R}_s = 1.4 \cdot 10^{-3}$ in the figure corresponds to $\mathcal{R}_s = 700$. The present figure reproduces Fig. 10 from [20] with the new convention for \mathcal{R}_s .

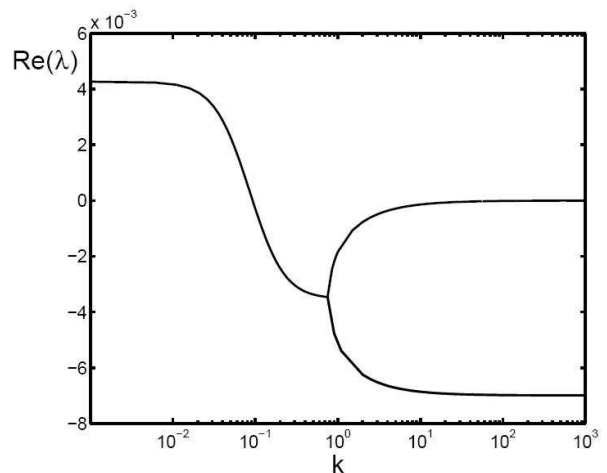


FIG. 3: Real part of the dispersion relation for $\mathcal{R}_s = 700$ and $\mathcal{U}_t = 23$.

Three values of \mathcal{R}_s are investigated, namely 700, 1400 and 7000. They correspond to $1/\mathcal{R}_s = 1.4 \cdot 10^{-3}$, $7 \cdot 10^{-4}$ and $1.4 \cdot 10^{-4}$. For these values, the dependence of the dispersion relation on the applied voltage \mathcal{U}_t was investigated. The stability of the $k=0$ -modes were found in Fig. 2, now also non-vanishing wave-numbers k are investigated.

For $\mathcal{R}_s = 700$, a generic shape of the dispersion relation is presented in Fig. 3. Here a very large range of k

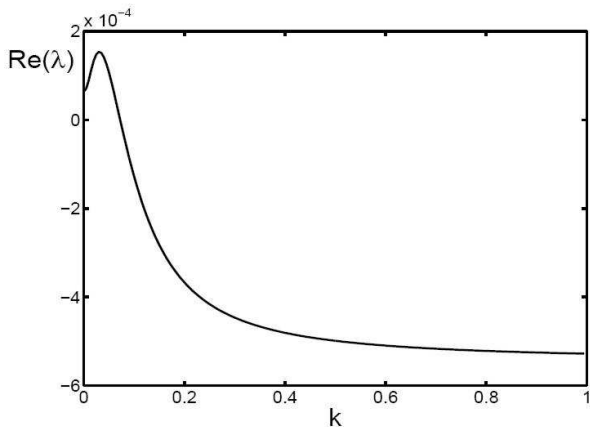


FIG. 4: Real part of the dispersion relation for $\mathcal{R}_s = 7000$ and $\mathcal{U}_t = 40$.

values is shown on a logarithmic scale. The mode with the largest growth rate $\text{Re } \lambda(k)$ is the one with vanishing wave number $k = 0$ that was already investigated in [20]. It is oscillating in time: $\text{Im } \lambda(k) \neq 0$.

For $k = \mathcal{O}(10^0)$, the two complex conjugate solutions $\lambda(k)$ in Fig. 3 merge and form two solutions with differing real part and vanishing imaginary part. If the upper solution would develop a positive growth rate $\text{Re } \lambda(k)$ for large k , we had found an exponentially growing, purely spatial instability with short wave length, but we haven't found such behavior. Variation of the applied voltage \mathcal{U}_t leads to qualitatively the same behavior: the temporally oscillating, but spatially homogeneous mode $k = 0$ has the largest growth rate and is oscillating in time. Whether this maximal growth rate is positive or negative, can be read from Fig. 2. The behavior for $\mathcal{R}_s = 1400$ is qualitatively the same.

Further increase of the semiconductor resistivity to $\mathcal{R}_s = 7000$ creates a new feature, namely a finite wave length instability: the growth rate becomes maximal for some non-vanishing, but very small value of $k = k^*$, as can be seen in Fig. 4.

In Fig. 5, this case is investigated further: the real and imaginary part of the two largest eigenvalues can be seen for a larger range of k . Up to $k \approx 8$, a pair of complex conjugate eigenvalues is found, then two different branches of purely real eigenvalues emerge. This behavior for larger k is the same as for smaller resistance \mathcal{R}_s .

Finally, Fig. 6 shows that the most unstable branch of eigenvalues approaches $\text{Re } \lambda(k) = 0$ from below for $k \rightarrow \infty$, but does not develop any positive growth rate. Clear evidence for positive growth rates of a purely real eigenvalue for large k has not been found when varying parameters of the system. If they would exist, they would indicate a purely growing spatial mode with short wave length.

The results of this section can be summarized as follows: within the upper part of Fig. 2, i.e., for small resis-

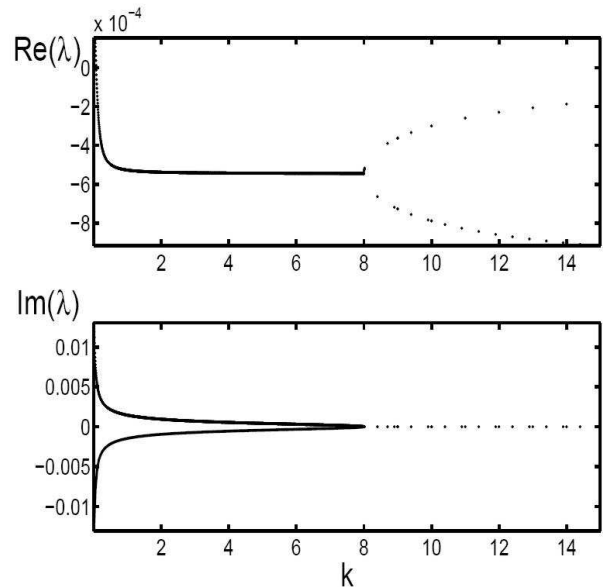


FIG. 5: Real and imaginary part of the two branches of the dispersion relation with largest growth rate for the same parameters as in Fig. 4.

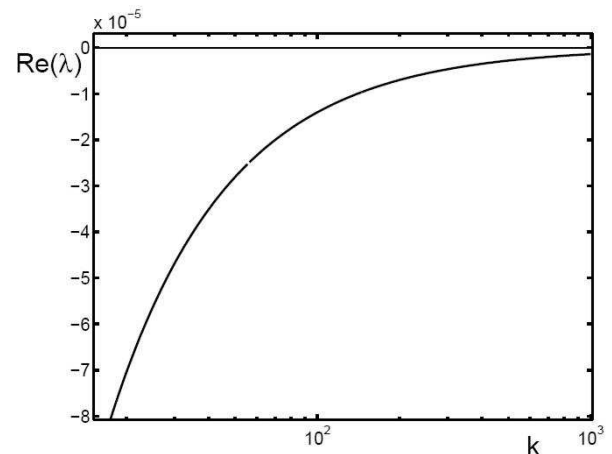


FIG. 6: Real part of the dispersion relation in the limit of $k \rightarrow \infty$ for the same parameters as in Figs. 4 and 5.

tivity \mathcal{R}_s , the results on spatially homogeneous temporal oscillations from [20] apply. In the lower part, the most unstable mode is oscillating as well, but it has a preferred finite wave length $k > 0$.

B. Dependence on gap lengths, resistance, and feeding voltage

We now investigate how these dispersion relations change when other system parameters are varied. When keeping material parameters like gas type and density

and the dielectricity constant of the semiconductor fixed, the following physical parameters can be varied: the widths L_s and L of the semiconductor and the gas layer, the externally applied voltage \mathcal{U}_t and the semiconductor resistance \mathcal{R}_s by a factor of 10 through photolumination.

Our idea is to start from one point in phase space (presumably always the same one) and then investigate influence of above listed physical parameters. Unfortunately, there are some limitations to this approach. First, parameter space is huge and therefore, it is practically impossible to systematically investigate all possibilities of dispersion relations behavior. Second, some of these parameters can not be changed independently. Still, we find it useful to present here examples on how different parameters influence dispersion relation with the purpose to give to experimentalist directions where to search for certain behavior of the system.

1. Dependence on L_s

In Fig. 7, we fixed conductivity $\sigma_s = 54/7000 = 7.714 \cdot 10^{-3}$ and varied L_s from 10 to 150 in equal steps, calculating then $\mathcal{R}_s \propto L_s$ and $C_s \propto 1/L_s$ according to equation (20) in the section II C. In physical units, the width of the semiconductor layer was changed from 0.27 mm to 4.16 mm. The other parameters we fixed were $J_0 = 1.32 \cdot 10^{-5}$ and $L = 36$, which, together with chosen σ_s , at $L_s = 54$ led to the parameters $\mathcal{R}_s = 7000$, $C_s = 0.243$ and $\mathcal{U}_t = 40$ as in the previous section in Figs. 4, 5 and 6.

Here for small L_s maximal growth rate is for $k = 0$ -mode, but with the increase in L_s , nonzero k becomes dominant mode, i.e. spatially homogeneous temporal instability shifts towards small k instability when increasing semiconductor width. It is also observed that in the case of Fig. 3, the most unstable mode can become nonzero when L_s is increased sufficiently.

For the standard width $L_s = 54$ the most unstable mode already had a nonvanishing wavenumber $k = k^*$, its growth rate $\text{Re } \lambda(k^*)$ slightly decreases with increasing L_s , approaching a certain limit, while its oscillation frequency $\text{Im } \lambda(k^*)$ increases. A decreasing L_s , on the other hand, can shift the most unstable mode back to vanishing wavenumber $k^* = 0$.

Increasing the width of the semiconductor layer actually means decreasing the capacitance of the system and increasing the resistivity and the necessary applied voltage. Consequently, all that may lead to long wave length instabilities.

2. Dependence on \mathcal{R}_s

In Fig. 8, resistance \mathcal{R}_s varies in the interval between 700 and 7000, at fixed $J_0 = 1.32 \cdot 10^{-5}$, while the other parameters are chosen as in the previous section: $L =$

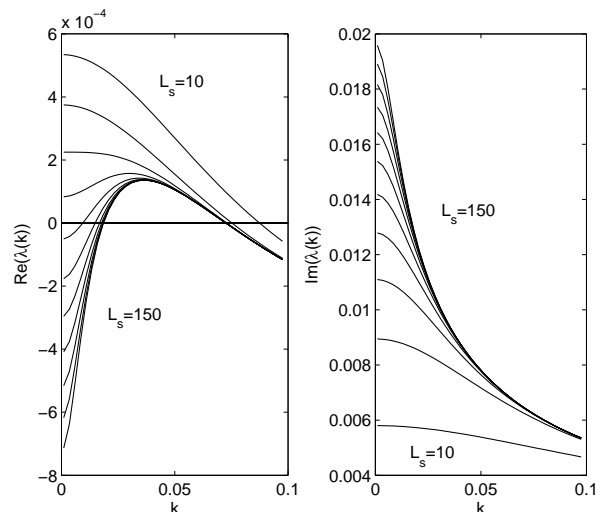


FIG. 7: The influence of the width L_s of the semiconductor layer on real and imaginary part of the dispersion relation $\lambda(k)$, for equidistant L_s from the range between $L_s = 10$ and 150 at $J_0 = 1.32 \cdot 10^{-5}$, $L = 36$. At $L_s = 54$, the parameters are as in Figs. 4, 5 and 6: $\mathcal{R}_s = 7000$, $C_s = 0.243$, and $\mathcal{U}_t = 40$.

36, $L_s = 54$, $C_s = 0.243$, and $\mathcal{U}_t = 40$ at $\mathcal{R}_s = 7000$. Therefore, the upper line in Fig. 8 for the $\mathcal{R}_s = 7000$ is the same as the one in Figs. 4, 5 and 6. This allows us to follow changes of dispersion relation when resistivity (and proportionally the feeding voltage) is decreased.

For smaller values of resistivity, growth rate $\text{Re } \lambda(k^*)$ is always negative, while for larger values we can expect spatially periodic pattern to emerge. Furthermore, for the smallest investigated \mathcal{R}_s ($\mathcal{R}_s = 700$), when $\mathcal{U}_t = 16.25$, growth rate is always negative as can be seen in Fig. 8, but when $\mathcal{U}_t = 23$, growth rate is positive (for the same k range) and has maximum for $k = 0$ as can be seen in Fig. 3.

Combining all observations lead to conclusion that in order to observe spatially periodic patterns one must search in the range of high resistivity and high feeding voltages.

3. Dependence on L

Fig. 9 shows for the same parameter values that with increasing gas gap width L , the growth rate $\text{Re } \lambda(k)$ increases and the oscillation frequency $\text{Im } \lambda(k)$ decreases, while the most unstable mode stays nonvanishing: $k^* > 0$.

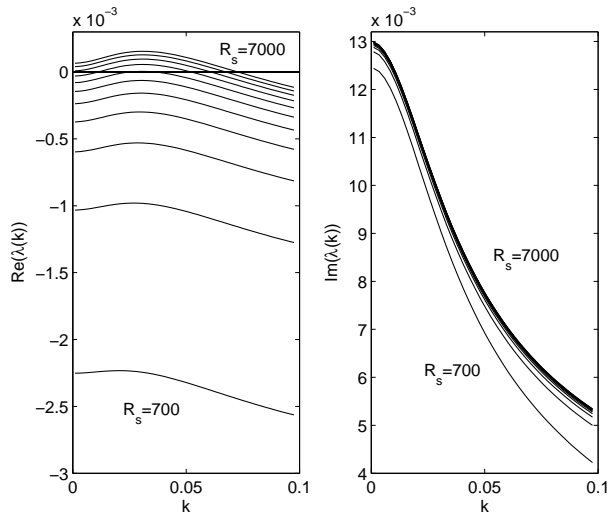


FIG. 8: The influence of the resistance \mathcal{R}_s of the semiconductor layer on real and imaginary part of the dispersion relation $\lambda(k)$ for equidistant \mathcal{R}_s from the range between $\mathcal{R}_s = 700$ and 7000. The current is $J_0 = 1.32 \cdot 10^{-5}$. All other parameters are as in Figs. 4, 5 and 6: $L = 36$, $L_s = 54$, $C_s = 0.243$, and $\mathcal{U}_t = 40$ at $\mathcal{R}_s = 7000$.

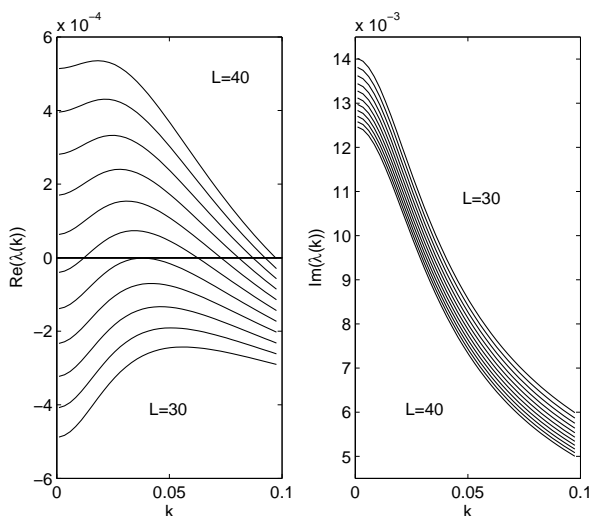


FIG. 9: The influence of the width L of the gas gap on real and imaginary part of the dispersion relation $\lambda(k)$ for $L = 30, 31, 32, \dots, 40$. The current is $J_0 = 1.32 \cdot 10^{-5}$. All other parameters are as in Figs. 4, 5 and 6: $\mathcal{R}_s = 7000$, $C_s = 0.243$, $L_s = 54$, and $\mathcal{U}_t = 40$ at $L = 36$.

4. Dependence on \mathcal{U}_t

Figure (10) shows how the most unstable wavenumber k^* and real and imaginary part of the corresponding eigenvalue depend on the feeding voltage \mathcal{U}_t at differ-

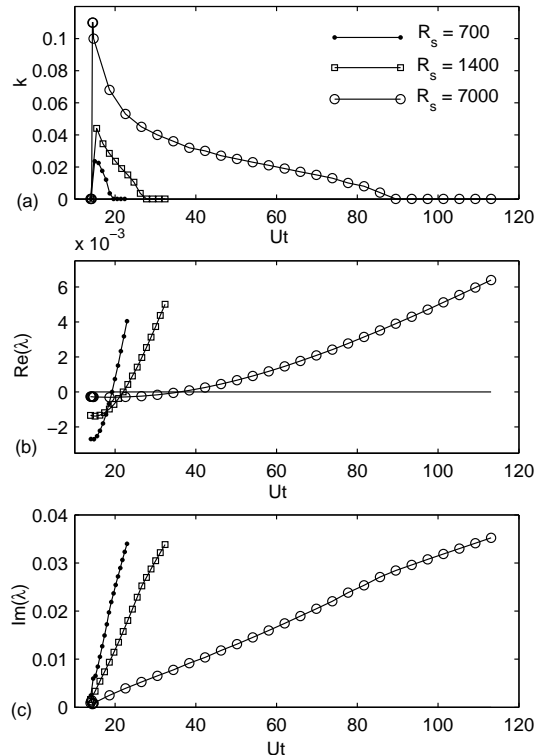


FIG. 10: (a) Most unstable wavenumber k , (b) real part and (c) imaginary part of the corresponding eigenvalue $\lambda(k)$ as a function of the total voltage \mathcal{U}_t for $\mathcal{R}_s = 700, 1400, 7000$. The change of \mathcal{R}_s can be achieved by photo-illumination.

ent dimensionless resistivities $\mathcal{R}_s = 700, 1400$ and 7000. The curves begin where the applied voltage \mathcal{U}_t equals the Townsend breakdown voltage [22, 23, 25].

Fig. (10)(a) shows that for small \mathcal{U}_t , the most unstable wavelength is always non-vanishing, and it decreases for growing \mathcal{U}_t until it vanishes exactly beyond some critical \mathcal{U}_t . Fig. (10)(b) shows that the growth rate $\text{Re } \lambda$ of the most unstable mode can still be negative in the range of dominant finite wave lengths. This explains why the finite wave length instabilities were not seen in Sect. IV A for small \mathcal{R}_s . In Fig. (10)(c), it can be seen that the most unstable modes are always oscillating in time.

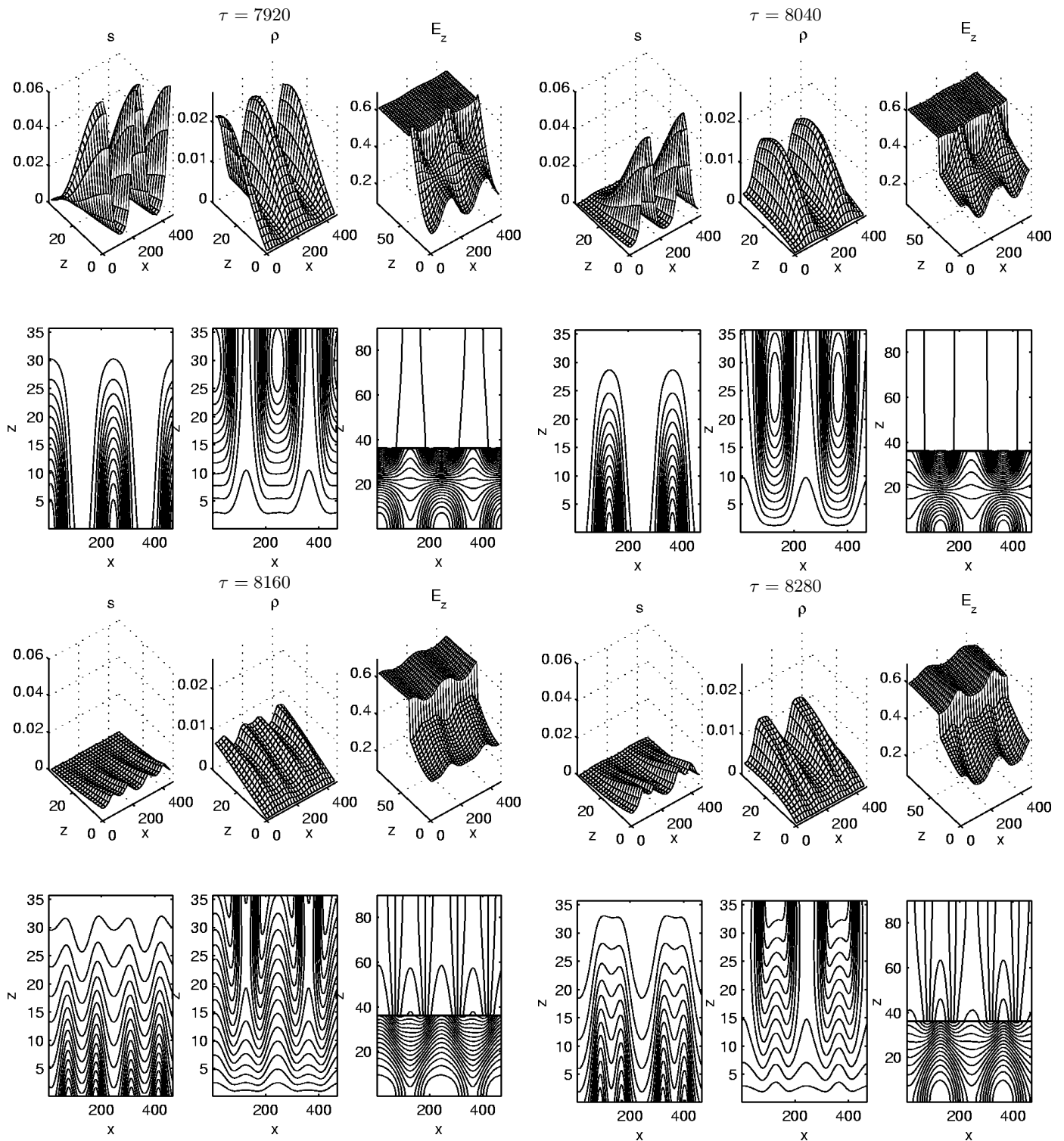


FIG. 11: Profiles and contour lines of electron and ion particle densities $s = \sigma/\mu$ and ρ in the discharge region, and electric field component E_z in discharge and semiconductor region at time steps $\tau = 7920, 8040, 8160, 8280$ for $U_t = 46.4$ and $\mathcal{R}_s = 7000$. x and z coordinates are as in Fig. 1 and the text. For each time step, the data is represented as a 3D plot in the upper row and as a contour plot in the lower row.

V. NUMERICAL SOLUTIONS OF THE INITIAL VALUE PROBLEM

A. Implementation and results

The full dynamical problem was also solved numerically as an initial value problem. This allows us on the one hand to test the results of the stability analysis, on the other hand, to study the behavior beyond the range of linear stability analysis. Details of the numerical implementation are given in the appendix.

We study the case of high resistivity $\mathcal{R}_s = 7000$ that leads to spatial pattern formation as discussed above. Two values of the applied potential were investigated: $\mathcal{U}_t = 23.7$ where the homogeneous stationary state is stable, and $\mathcal{U}_t = 46.4$ where this state is unstable and the fastest growing mode is an oscillating one with finite wavenumber k^* .

In the transversal direction, we use periodic boundary conditions. We choose the lateral extension L_x as a multiple of the most unstable wave length $2\pi/k^*$. After some tests with higher multiples showing essentially the same behavior, we used $L_x = 2 \times 2\pi/k^*$. The initial condition is

$$\rho(x, z, 0) = \rho_0(z) + C \rho_1(z) e^{ik^*x} + \text{c.c.}, \quad (67)$$

where k^* is the wavenumber of the most unstable mode, $\rho_0(z)$ is the stationary solution, and $\rho_1(z)$ is the eigenfunction for $k = k^*$ constructed in Sect. III C. The constant C is chosen such that the perturbation is small compared to $\rho_0(z)$. Note that we need to specify the initial conditions for the ion density only, since electron density and field are determined by it.

Figure 11 shows about one period of oscillation within 4 time steps for the pattern forming case ($\mathcal{U}_t = 46.4$). For each instant of time, the rescaled electron density $s = \sigma/\mu$ and the ion density ρ are shown in the gas discharge region, and the electric field is shown both in the gas discharge and the semiconductor region. The upper row contains 3D plots and the lower row contour plots. The figures show the characteristic electron and ion distribution of a glow discharge, but with a strong spatio-temporal modulation.

The temporal period predicted by linear perturbation theory is 528. This agrees approximately with the numerical results. On the other hand, the destabilization of the homogeneous stationary state in Fig. 11 is already far developed and in the fully nonlinear regime. Therefore the results of the stability theory at this time give only an indication for the full behavior. In particular, the nonlinearity has created an onset to doubling the spatial period that is absent for small perturbations.

For presenting the evolution in time, the spatial structure has to be represented on a line rather than in the full (x, z) -plane. Obviously, the ion density on the semiconductor-gas-interface (x, L) is an appropriate quantity, since it characterizes the local intensity of the discharge glow in the transversal direction. Figures 12

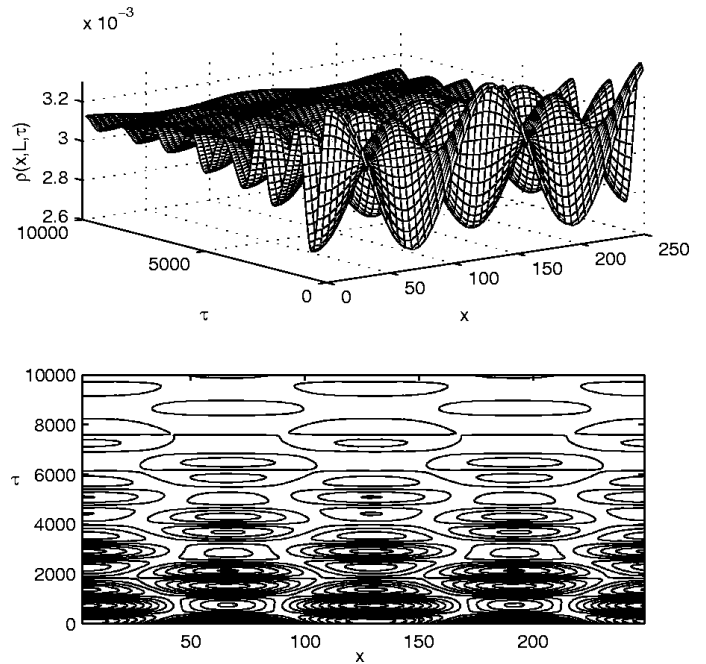


FIG. 12: Evolution of ion density at the internal border $z = L$ for $\mathcal{U}_t = 23.7$ and $\mathcal{R}_s = 7000$ as a function of the transversal coordinate x and time τ . Note that time τ increases towards the back.

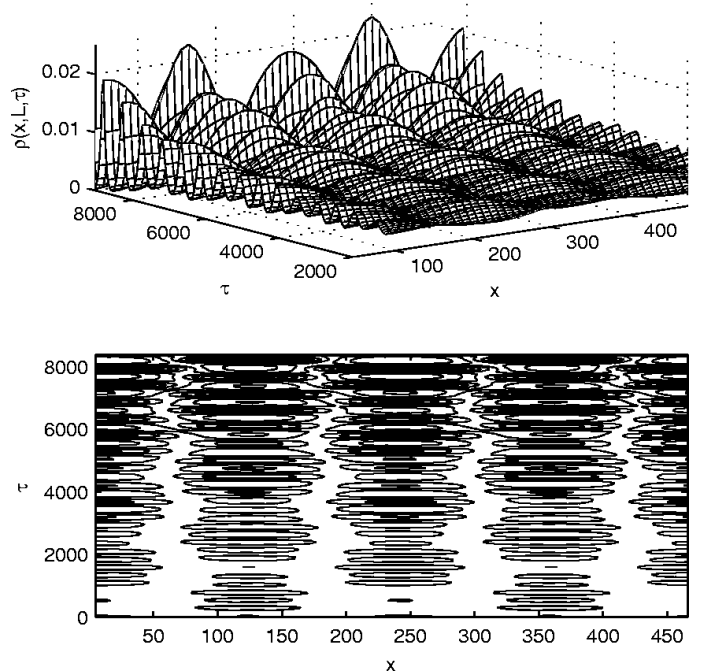


FIG. 13: The same as in the previous figure, but now for $\mathcal{U}_t = 46.4$. Temporal snapshots in the full (x, z) -plane of the same numerical experiment can be found in Fig. 11.

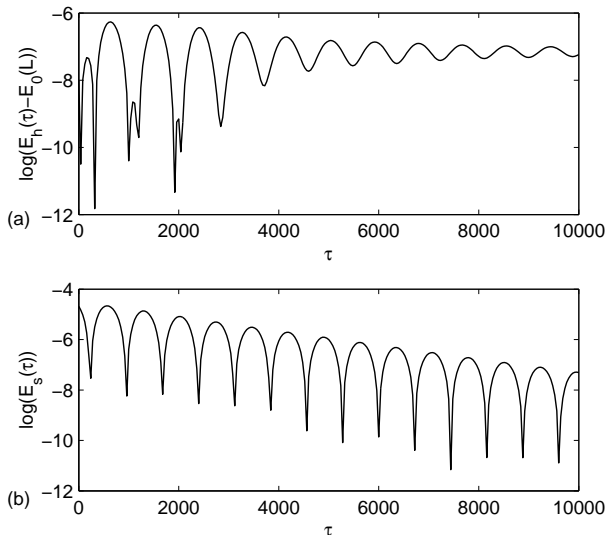


FIG. 14: Temporal evolution of the transversally averaged electric field and of the spatial modulation of the field at the internal border $z = L$ for $\mathcal{U}_t = 23.7$ and $\mathcal{R}_s = 7000$: (a) $\log(\mathcal{E}_h(\tau) - \mathcal{E}_0(L))$ and (b) $\log \mathcal{E}_s(\tau)$ as a function of τ .

and 13 show the complete temporal evolution in such a presentation. Fig. 12 presents data of a perturbation decaying towards the stationary homogeneous state for $\mathcal{U}_t = 23.7$, while Fig. 13 shows the growing destabilization of the homogeneous stationary state for $\mathcal{U}_t = 46.4$; the late stage of this evolution was shown in Fig. 11.

B. Comparison of numerical and stability results

When one wants to compare results of the numerical simulation and of the stability analysis, the evolution of different spatial modes has to be extracted from the simulation. Appropriate quantities are the transversally averaged electric field on the gas-semiconductor interface

$$\mathcal{E}_h(\tau) = \frac{1}{L_x} \int_0^{L_x} \mathcal{E}_z(L, x, \tau) dx, \quad (68)$$

and the spatial modulation of the field

$$\mathcal{E}_s(\tau) = \max_x \mathcal{E}_z(L, x, \tau) - \min_x \mathcal{E}_z(L, x, \tau). \quad (69)$$

These quantities, or rather the logarithms of $\mathcal{E}_h(\tau) - \mathcal{E}_0(L)$ and of $\mathcal{E}_s(\tau)$ are shown for the stabilizing case $\mathcal{U}_t = 23.7$ in Fig. 14, and for the destabilizing case $\mathcal{U}_t = 46.4$ in Fig. 15.

In this logarithmic plot for the fields, the lines through the maxima are approximately straight, which means that the growth is exponential. For the destabilizing case, the growth rate of the spatial mode $\mathcal{E}_s(\tau)$ is slightly larger

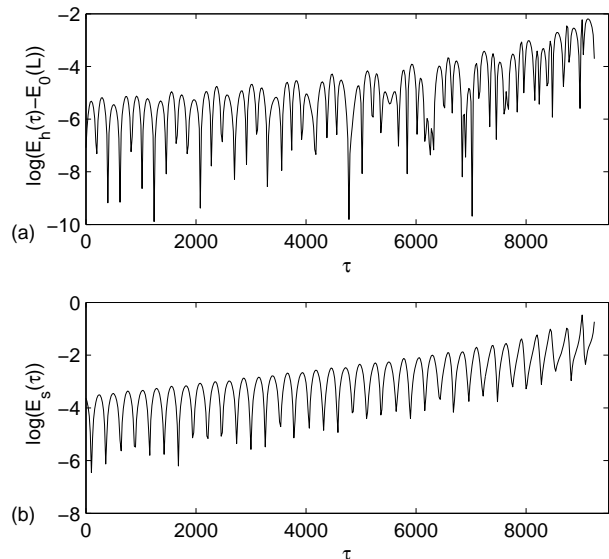


FIG. 15: The same as in the previous figure, now for $\mathcal{U}_t = 46.4$.

than that of the homogeneous mode $\mathcal{E}_h(\tau)$ which implies that the most unstable mode has a non-vanishing wave number k^* : $\text{Re}[\lambda(k^*)] > \text{Re}[\lambda(0)]$. Furthermore, at late stages when the dynamics is beyond the range of linear perturbation theory and becomes nonlinear, the growth of all modes accelerates.

Figs. 16 and 17 show a quantitative comparison between stability analysis and computational results. Fig. 16 shows the stabilizing case $\mathcal{U}_t = 23.7$. The stability analysis predicts that $k^* = 0.050$ is the most unstable mode; it has the eigenvalue $\lambda(k^*) = -0.2807 \cdot 10^{-3} + 0.4320 \cdot 10^{-2}i$. Therefore, the period of the temporal oscillations is predicted as $2\pi/\text{Im}(\lambda) = 1454$, the characteristic decay time as $1/\text{Re}(\lambda) = 3563$, and the characteristic wave length as $2\pi/k^* = 126$. This predicted behavior is shown as the dashed line in the upper panel of Fig. 16. The solid lines show the numerical solution, more precisely the time evolution of the ion density $\rho(x, L, \tau)$ evaluated on the grid nodes in the range between $x = 0$ and $x = L_x/4$ on the gas-semiconductor interface $z = L$. Period and growth rate agree quantitatively, therefore both simulations and stability analysis can be trusted.

The predictions on the $k=0$ -mode are tested in the lower panel of Fig. 16: here the transversal extension of the simulation system was chosen so narrow that transversal modes had no space to develop: the width was taken as $L_x = 2\pi/(100k^*)$ where k^* is the most unstable wave length. In this case, only the $k = 0$ -mode can grow, it has $\lambda(0) = -0.3547 \cdot 10^{-3} + 0.7102 \cdot 10^{-2}i$. The plot again shows a very good agreement between stability analysis and simulation, now effectively for the one-dimensional case.

Finally, in Fig. 17 again the destabilizing state for $\mathcal{U}_t =$

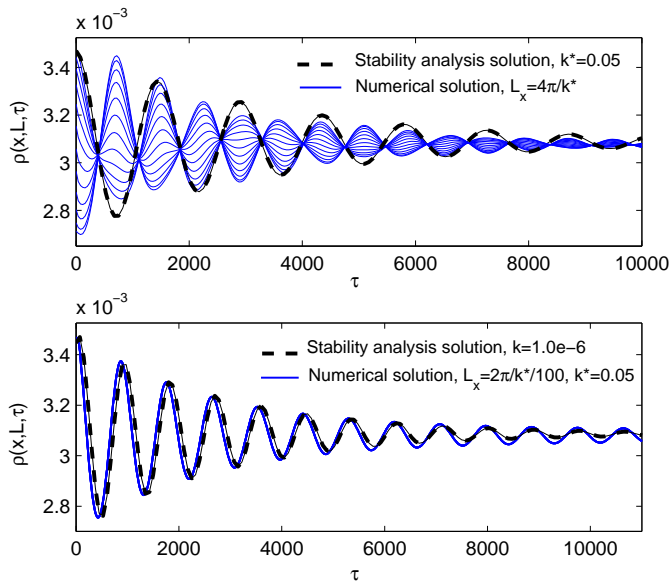


FIG. 16: (Color online) Comparison of results of the PDE solutions (solid lines) and of the stability analysis (dashed line). Ion density ρ at the computational nodes between $x = 0$ and $x = L_x/4$ of the internal border $z = L$ as a function of time for $\mathcal{U}_t = 23.7$ and $\mathcal{R}_s = 7000$.

46.4 is shown. The stability analysis predicts the most unstable wave number $k^* = 0.0267$ and its eigenvalue $\lambda(k^*) = 0.4615 \cdot 10^{-3} + 0.1191 \cdot 10^{-1} i$. The two panels show again the predicted and the simulated oscillations in a laterally wide system allowing the formation of the k^* -mode, and in the narrow system that only has space for the $k=0$ -mode. Again, the agreement is convincing.

At this point, the numerical calculations are tested. This should be the starting point for new simulation predictions in the nonlinear regime that are not accessible by stability analysis.

VI. CONCLUSIONS AND DISCUSSIONS

We have investigated the spatio-temporal pattern formation in a semiconductor-gas discharge system with the simplest model possible. Only the drift motion of electron and ion densities is taken into account, and the electrons are adiabatically eliminated. The semiconductor is approximated as a linear Ohmic conductor, and nonlinear effects come in only through the space charges of the ions in the gas discharge gap and through the surface charges on the gas-semiconductor interface.

Results of the linear stability analysis of the homogeneous stationary state and of the full numerical simulation of the initial value problem are presented. The choice of parameters is guided by the experiment described in [4]; they are summarized in Sect. II E. In the experiment [4], the resistance of the semiconductor can be changed

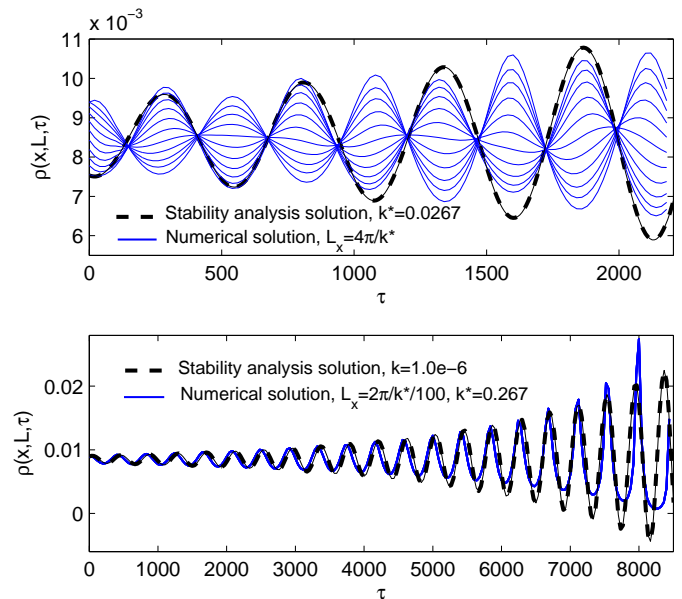


FIG. 17: (Color online) The same as in the previous figure, now for $\mathcal{U}_t = 46.4$.

by a factor of 10 by photo-illumination without changing any other system parameter. It is seen that the system never relaxes to a spatially structured time-independent state, but depending on the resistance, it either forms a homogeneous oscillating or a spatially structured oscillating state. These spatially structured oscillating states actually appear at high resistivity of the semiconductor layer.

The results of our stability analysis agree with these experimental observations: no unstable modes at a large wavenumber k were observed where the instability would be purely growing ($\text{Im}(\lambda(k))=0$) and finally saturating. All most unstable modes were oscillating and had a small or vanishing wave number k . Furthermore, when increasing the applied voltage \mathcal{U}_t for fixed $\mathcal{R}_s = 700$ or 1400 , a spatially homogeneous temporal instability occurred, while for the large resistivity $\mathcal{R}_s = 7000$, it was spatially structured, in agreement with experiments. Furthermore, the thesis [6] reports that when increasing the voltage \mathcal{U}_t for fixed large resistance \mathcal{R}_s , first a state with wide “diffuse” moving bands occurs, before the blinking filaments described in [4] set in. These stripes are likely to correspond to the instabilities with large wave length $2\pi/k^*$ predicted by our stability analysis, though no experimental data is available that would allow a quantitative comparison. It is interesting to note that the physical mechanism of these “diffuse” bands has nothing to do with particle diffusion, but only with the Laplacian nature of the created electric fields. For further predictions on the parameter dependence of the linear instability, we refer to Section IV B.

Finally, our numerical solutions of the initial value

problem show good agreement with linear stability analysis within its range of validity. First of all, this proves the correct implementation of both methods. Second, for larger amplitudes, new spatial structures appear such as the spatial period doubling in Fig. 11. For $\mathcal{R}_s = 7000$ and $\mathcal{U}_t = 40$, these oscillations actually have been seen to reach a limit cycle that corresponds to a standing wave. Of course, it should be noted that the 2D approach is only justified in the regime of linear stability theory. Nevertheless our 2D-calculations also give a qualitative picture of the full nonlinear 3D dynamics.

We remark finally that only the simplest possible model with nonlinear space charge effects was investigated. Of course, the model can be extended by various additional effects, but obviously the simple model already contains all relevant physics to predict the onset of pattern formation in the experimental system.

Acknowledgments

The authors are grateful to Alexander Morozov from Instituut-Lorentz, Leiden University for his important contribution to this work. He pointed out the correct numerical strategy for shooting eigen values at large wavenumbers and helped implementing the method. I. Rafatov acknowledges numerous discussions with W. Hundsdorfer at the Center for Mathematics and Computer Science (CWI) Amsterdam on numerical mathematics. He also acknowledges support by ERCIM and FOM during his work in Amsterdam, and D.D. Sijacic acknowledges support by FOM for work in Amsterdam where the numerical stability analysis was performed and the numerical PDE work was initiated.

APPENDIX A: NUMERICAL PROCEDURE

Here we describe the numerical method used for solving the initial value problem numerically. The computation is based on a finite-difference technique to solve equations (24)–(26) with boundary conditions (27)–(30) and periodic boundary conditions in the transversal direction.

The computational domain is a rectangular region $[0, L_x] \times [0, L_z]$ on a two-dimensional Cartesian coordinate system (x, z) , which consists of two layers – gas and semiconductor, see Figs. 1 and 18. We use a uniform vertex-centered grid in the 'vertical' z -direction with nodes

$$z_j = j\Delta z, \quad \Delta z = \frac{L_z}{N}, \quad j = 0, 1, \dots, N$$

and a uniform cell-centered grid with nodes

$$x_i = \left(i - \frac{1}{2}\right) \Delta x, \quad \Delta x = \frac{L_x}{M}, \quad i = 1, 2, \dots, M$$

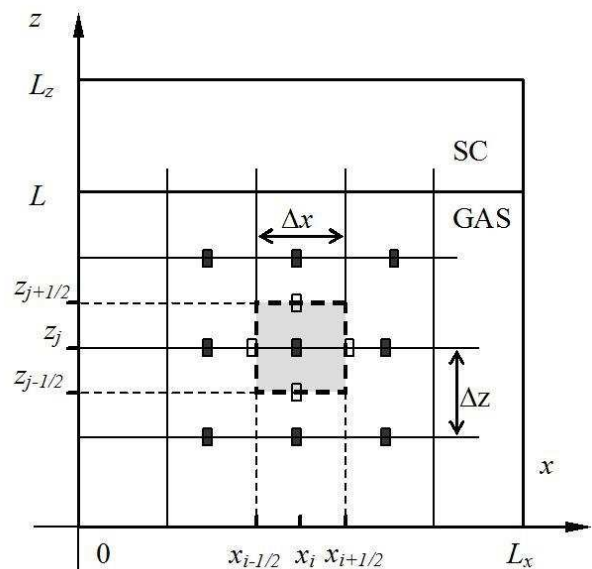


FIG. 18: Computational domain and computational cell.

on the 'horizontal' x -direction. The grid is spaced such that the internal interface between semiconductor and gas region lies exactly on the grid line.

The densities $s = \sigma/\mu$ and ρ and the electric potential ϕ are evaluated on the nodes of the grid, while the x and z components of the electric field (\mathcal{E}_x and \mathcal{E}_z , respectively) are calculated on the surfaces of the computational cell (Fig. 18).

To obtain a finite-difference representation of equations (24) and (25), we first integrate them over the cell volume $x_{i-1/2} \leq x \leq x_{i+1/2}$, $z_{j-1/2} \leq z \leq z_{j+1/2}$. Let us consider in detail the equation for the ions (25). After its integration, we come to

$$\frac{d\rho_{j,i}}{d\tau} = \frac{(\mathcal{E}_x \rho)_{j,i-1/2} - (\mathcal{E}_x \rho)_{j,i+1/2}}{\Delta x} + \frac{(\mathcal{E}_z \rho)_{j-1/2,i} - (\mathcal{E}_z \rho)_{j+1/2,i}}{\Delta z} + f_{j,i}. \quad (\text{A1})$$

The subscripts i and j are related to x (transversal) and z (longitudinal) directions respectively and f stands for the source term of Eq. (25).

The choice of $\rho_{j\pm 1/2,i}$ and $\rho_{j,i\pm 1/2}$ at the surfaces of the computational cell determines the concrete discretization method for the convective terms of Eq. (25). We used the third-order upwind-biased scheme (see, e.g., [28], p. 83),

which in z - and x -direction is given by

$$\begin{aligned} (\mathcal{E}_z \rho)_{j+1/2,i} &= \frac{1}{6} \left[\mathcal{E}_z^+_{j+1/2,i} (-\rho_{j-1,i} + 5\rho_{j,i} + 2\rho_{j+1,i}) \right. \\ &\quad \left. + \mathcal{E}_z^-_{j+1/2,i} (2\rho_{j,i} + 5\rho_{j+1,i} - \rho_{j+2,i}) \right], \\ (\mathcal{E}_x \rho)_{j,i+1/2} &= \frac{1}{6} \left[\mathcal{E}_x^+_{j,i+1/2} (-\rho_{j,i-1} + 5\rho_{j,i} + 2\rho_{j,i+1}) \right. \\ &\quad \left. + \mathcal{E}_x^-_{j,i+1/2} (2\rho_{j,i} + 5\rho_{j,i+1} - \rho_{j,i+2}) \right]. \end{aligned} \quad (\text{A2})$$

Here, the electric field components are

$$\mathcal{E}_{\dots}^+ = \max \left[0, \mathcal{E}_{\dots} \right], \quad \mathcal{E}_{\dots}^- = \min \left[0, \mathcal{E}_{\dots} \right],$$

and $\mathcal{E} = -\nabla\phi$ is discretized as

$$\begin{aligned} \mathcal{E}_z_{j+1/2,i} &= -\frac{\phi_{j+1,i} - \phi_{j,i}}{\Delta z}, \\ \mathcal{E}_x_{j,i+1/2} &= -\frac{\phi_{j,i+1} - \phi_{j,i}}{\Delta x}. \end{aligned} \quad (\text{A3})$$

For the numerical time integration, we used the extrapolated second order BDF2 method, see [28], p. 204, [29], p. 197, whose variable step size version has the form

$$\begin{aligned} \rho^m - \frac{(1+r)^2}{1+2r} \rho^{m-1} + \frac{r^2}{1+2r} \rho^{m-2} \\ = \frac{(1+r)}{1+2r} \Delta\tau_m (2F^{m-1} - F^{m-2}), \quad m \geq 2, \end{aligned} \quad (\text{A4})$$

where the superscript m denotes the time τ_m with step size $\Delta\tau_m = \tau_m - \tau_{m-1}$ and step size ratio $r = \Delta\tau_m / \Delta\tau_{m-1}$. Here F contains the discretized convective terms and a source term. Note that we have dropped spatial indices in Eq. (A4). Since the two-step method needs ρ^0 and ρ^1 as starting values, the explicit Euler method

$$\rho^m = \rho^{m-1} + \Delta\tau_m F(\tau_{m-1}, \rho^{m-1}) \quad (\text{A5})$$

is used for the first step $m = 1$. Because of the explicit time integration, we are restricted by the standard CFL stability condition.

The same space discretization technique and time integration method are used also for the electron density

equation (24) that contains no temporal derivative. Note that in this case the z -direction plays the role of 'time' in (A4) and (A5).

To obtain a finite-difference approximation for Poisson's equation (26), we use the traditional second order discretization:

$$\begin{aligned} -\frac{\phi_{j,i-1}^m - 2\phi_{j,i}^m + \phi_{j,i+1}^m}{(\Delta x)^2} - \frac{\phi_{j-1,i}^m - 2\phi_{j,i}^m + \phi_{j+1,i}^m}{(\Delta z)^2} \\ = \begin{cases} 0, & \text{gas-discharge layer,} \\ \rho_{j,i}^{m-1}, & \text{semiconductor layer.} \end{cases} \end{aligned} \quad (\text{A6})$$

This equation is valid everywhere except at the gas semiconductor interface where one has to account for a finite surface charge as well as for a discontinuity of the dielectricity constant. On this interface, the discrete version of the 'jump' condition (29) is used instead of (A6). The system of resulting difference equations is solved by a symmetrical successive over-relaxation method (SSOR), see [30], p. 343.

The complete numerical procedure was organized as follows. For every new $(m+1)$ th time step, first Poisson's equation was solved using the known ion density ρ^m and surface charge value q_b^m in the jump condition (29), determining the electric field components in the new time step. Second, the electron density in the new time step s^{m+1} was calculated. This determined the source term in the continuity equation for ions. Third the ion density ρ^{m+1} was calculated, which finally determined the new value for the surface charge in (29).

The numerical convergence was checked by performing several calculations with different error tolerance parameters for Poisson's equation, using refinement of the space grid, and different time stepping parameters. The number of grid nodes used in the calculations was 52×361 in the x and z directions, respectively, for the potential in the whole gas discharge - semiconductor region, and 54×147 in the x and z directions for the particle densities in the gas discharge region. When solving Poisson's equation, the iteration process is stopped when the relative error is $\|\phi^{(k+1)} - \phi^{(k)}\| / \|\phi^{(k+1)}\| < 5 \cdot 10^{-7}$.

[1] M.C. Cross and P.C. Hohenberg, Rev. Mod. Phys. **65**, 851–1112 (1993).
 [2] C. Strümpel, Y.A. Astrov, E. Ammelt, and H.-G. Purwins, Phys. Rev. E **61**, 4899 – 4905 (2000).
 [3] C. Strümpel, Y.A. Astrov, and H.-G. Purwins, Phys. Rev. E **62**, 4889 – 4897 (2000).
 [4] C. Strümpel, H.-G. Purwins, and Y.A. Astrov, Phys. Rev. E **63**, 026409 (2001).
 [5] C. Strümpel, Y.A. Astrov, and H.-G. Purwins, Phys. Rev. E **65**, 066210 (2002).

[6] C. Strümpel. Ph.D. thesis, Univ. Münster, Germany, 2001.
 [7] Yu.A. Astrov, E. Ammelt, S. Teperick, and H.-G. Purwins, Phys. Lett. A **211**, 184 (1996).
 [8] Yu.A. Astrov, E. Ammelt, and H.-G. Purwins, Phys. Rev. Lett. **78**, 3129 (1997).
 [9] Yu.A. Astrov and Y. A. Logvin, Phys. Rev. Lett. **79**, 2983 (1997).
 [10] E. Ammelt, Yu.A. Astrov, and H.-G. Purwins, Phys. Rev. E **55**, 6731 (1997).

- [11] Y.A. Astrov, I. Müller, E. Ammelt, and H.-G. Purwins, Phys. Rev. Lett. **80**, 5341 (1998).
- [12] E.Ammelt, Yu.A. Astrov, and H.-G. Purwins, Phys. Rev. E **58**, 7109 (1998).
- [13] Y.A. Astrov and H.-G. Purwins, Phys. Lett. A **283**, 349 (2001).
- [14] E.L. Gurevich, A.S. Moskalenko, A.L. Zanin, and H.-G. Purwins, Phys. Lett. A **307**, 299 (2003).
- [15] E.L. Gurevich, Yu.A. Astrov, and H.-G. Purwins, J.Phys.D: Appl.Phys. **3**, 468 2005
- [16] U. Kogelschatz, Plasma Chem. Plasma Process, **23**, 1 (2003).
- [17] W. Breazeal, K.M. Flynn, and E.G. Gwinn, Phys. Rev. E **52**, 1503 (1995).
- [18] Y.P. Raizer, E.L. Gurevich, and M.S. Mokrrov, Sov. Phys. Tech. Phys. **51**, 185 (2006)
- [19] D.D. Šijačić, U. Ebert, and I. Rafatov, Phys. Rev. E **70**, 056220 (2004).
- [20] D.D. Šijačić, U. Ebert, and I. Rafatov, Phys. Rev. E **71**, 066402 (2005).
- [21] U. Ebert, W. van Saarloos, and C. Caroli, Phys. Rev. E **55**, 1530 (1997).
- [22] D.D. Šijačić and U. Ebert, Phys. Rev. E **66**, 066410 (2002).
- [23] Yu.P. Raizer, U. Ebert, and D.D. Šijačić, Phys. Rev. E **70**, 017401 (2004).
- [24] A. von Engel and M.Steenbeck, *Elektrische Gasentladungen* (Springer, Berlin, 1934), Vol. II.
- [25] Y.P. Raizer, *Gas Discharge Physics* (Springer, Berlin, 2nd corrected printing, 1997).
- [26] S. Godunov, Uspekhi Mat. Nauk. **16**, 243-255 (1961).
- [27] S.D. Conte, SIAM Review **8**, 309-321 (1966).
- [28] W. Hundsdorfer and J.G. Verwer, *Numerical solution of time-dependent advection-diffusion-reaction equations*, Springer Series in Computational Mathematics **33** (Springer, Berlin, 2003).
- [29] P. Wesseling, *Principles of computational fluid dynamics*, Springer Series in Computational Mathematics **29** (Springer, Berlin, 2001).
- [30] J.W. Thomas, *Numerical Partial Differential Equations: Conservation Laws and Elliptic Equations*, Texts in Applied Mathematics **33** (Springer, Berlin, 1999).